Available online at www.sciencedirect.com
SCIENCE DIRECT®
International Journal of Solids and Structures 42 (2005) 1401–1424
INTERNATIONAL JOURNAL OF SOLIDS and STRUCTURES
www.elsevier.com/locate/ijsolstr

Micromechanical modeling of ductile cast iron incorporating damage. Part I: Ferritic ductile cast iron

Nicola Bonora *, Andrew Ruggiero

DiMSAT—Department of Mechanics, Structures and Environment, University of Cassino, Via G. Di Biasio 43, I-03043 Cassino, Italy

Received 29 June 2004; received in revised form 16 July 2004
Available online 18 September 2004

Abstract

The market for ductile cast iron as a substitute material increases every year. The material structural performance is strongly dependent on the microstructure. Micromechanics can help in understanding the role played by the microstructure constituents as well as the effects associated to the shape of the spheroids, their density, surface roughness, etc. The potential of application for micromechanics modeling can be further increased if features such damage mechanics and residual stresses are incorporated. In this paper, a micromechanics modeling approach based on the unit cell development has been developed paying particular attention to the role and the behavior of the constituents. Residual stresses, resulting from the cooling down to room temperature, have been demonstrated to be critical for an accurate prediction of the non-linear behavior of the DCI in the early deformation range. As far as damage mechanics is concerned, it has been demonstrated that voids nucleating from debonded spheroids are not sufficient to explain catastrophic failure at the macroscale while the occurrence of additional ductile damage in the matrix material is the driving process for rupture in ferritic DCI.

Keywords: Ductile cast iron; Ductile damage; Residual stresses; Ferrite; Graphite

1. Introduction

Every year, ductile cast irons (DCI) find new fields of application, as steel substitute material, mainly as a result of their good properties that, in most of the cases, are even better than those of low carbon steels.

* Corresponding author. Tel.: +39 0776299 3693; fax: +39 0776299 3390.
E-mail address: nbonora@unicas.it (N. Bonora).

0020-7683/$ - see front matter © 2004 Elsevier Ltd. All rights reserved.
doi:10.1016/j.ijsolstr.2004.07.025

Nomenclature

D	damage
D^+	active damage
D_0	initial damage
D_{cr}	critical damage at failure
E_0	initial Young's modulus
E	actual Young's modulus for the damaged material
E_g	graphite Young modulus
E_{ij}	meso-strain components
F_D	damage dissipation potential
F_p	plasticity dissipation potential
F_{ij}	cell resulting reaction forces
L_0	reference unit cell length
Y	elastic damage strain energy release rate
S_0	material constant
P	pressure, hydrostatic part of the stress tensor
R	actual cell radius
R_0	initial cell radius
K	isotropic hardening back stress
TF	triaxiality factor
p	total equivalent accumulated plastic strain under multiaxial state of stress
p^+	active total equivalent plastic strain accumulated under tension only
p_{th}	plastic strain threshold under multiaxial state of stress
p_f	plastic strain at failure under multiaxial state of stress (ductility)
s_{ij}	deviatoric stress tensor
α	damage exponent
ε_{th}	damage strain threshold
ε_f	failure strain under uniaxial state of stress (TF = 0.333)
λ	plastic multiplier
ν	Poisson's ratio
κ	isotropic hardening internal variable
σ_m	hydrostatic stress
σ_{eq}	equivalent von Mises stress
Σ_{ij}	meso-stress components

Castability, cast dimension stability, together with a relatively high ductility (up to 25% for ferritic grades) are critical characteristics, especially from the economical point of view, for the use of DCI in the applications.

DCI microstructure shows suitably dispersed graphite spheroids in the ferrous matrix, which can spread from purely ferritic to perlitic microstructure according to the cooling rate and heat treatment. More recently austempered DCI family has been also introduced in the market (Jenkins, 1984). The presence of two distinct phases, i.e. particles embedded into a matrix, makes this material conceptually a "natural" composite, (Labrecque and Cagné, 1998) for which the overall resulting properties at the macroscale can be predicted by means of micromechanics analysis.

Even though DCI technology has been developed since 1948, the number of papers addressing the possibility to accurately predict resulting macroscopic constitutive response from a computational point of view, as well as constituents interactions and geometric related effects, today, is still very limited.

In most of the papers presented in the literature, DCI microstructure is schematized as simple voided matrix for which Gurson-like constitutive modeling seems to perform well (Steglich et al., 1996; Zhang et al., 1999; Berdin and Haušild, 2002; Liu et al., 2002). In this framework the role of spheroids is completely neglected on the consideration that, due to the "soft" nature of these particles, the contribution to the resulting material stiffness is either limited or completely insignificant. In addition to this, the material in the micromechanical analysis is always assumed to be stress free at the temperature at which the study is performed, usually room temperature (RT), without any concern with the effective stress/strain state in the microstructure.

Micromechanics is a powerful computational tool that gives the resulting properties of the material at the macro-scale, from known characteristics of the constituents and microstructure topology, through the analysis of periodic representative volume element (RVE) or the development of a unit cell model (UCM) (Adams and Crane, 1984; Allen and Boyd, 1993). This approach not only allows one to calculate material response in both elastic and plastic regimes but, if damage mechanisms are accounted for, also to predict the occurrence of catastrophic failure under varying loading conditions and triaxiality stress states. Micromechanics approach has been widely used to predict macroscale constitutive behavior of composites. Hashin and Shtrikman (1963) and Hashin and Rosen (1964) derived the upper and lower bound for the elastic constants using energy variational principles. Aboudi (1989) derived a micromechanics framework for periodic cells able to predict both elastic and inelastic behavior. More recently, Sun and Vaidya (1996) investigated the problem related to the application of periodical boundary conditions in predicting shear moduli. Today, micromechanics approach largely relies on finite element method (FEM) since non-linearities in the constituents behavior can be easily accounted for as well as temperature changes, plasticity, damage, etc. Bonora et al. (1994) and Bonora and Ruggiero (2004a) developed a unit cell based approach to predict constitutive response of unidirectional metal matrix (SiC/Ti-15-3) laminates emphasizing the importance to incorporate in the simulation the manufacturing process and the damage mechanics.

The role of the manufacturing process is critical for those composites in which the interface bond between the matrix and the reinforcement is mechanical. In these materials, the matrix shrinks around the reinforcement due to the thermal expansion coefficients mismatch during the cooling phase down to the room temperature. Similar situation occurs for the DCI. Slightly below the eutectic temperature ($\approx$1150 °C) matrix and eutectic nodules are created as a matter of fact simultaneously. Below this temperature, the number (i.e. nodule counts), the dimension and shape of the nodules are remaining practically constant. Thus, the resulting interface between the nodule and the matrix, which has a α-thermal expansion coefficient at least one order of magnitude higher than that of the graphite, develops according to the cooling path and the rate.

Starting from these considerations, a micromechanical methodology for DCI based on unit cell analysis has been developed. The study addresses manifold aspects which have critical effect on the effective predicting capabilities of UCM, such as the damage mechanism for the matrix type, the role of the residual stresses and strain resulting from the cooling down process, the spheroid effective shape and its constitutive response, the effect of stress triaxiality on the expected ductility. The results of this extensive research have been organized in three papers: in the present one the proposed UCM methodology is applied to purely ferritic DCI. Here, a continuum damage mechanics (CDM) model for the ductile matrix is developed and the damage parameters have been identified. In Part II, (Bonora and Ruggiero, 2004b), the proposed approach is applied to purely perlitic DCI, for which local approach to fracture has been used to predict brittle fracture and the associated experimental scatter. In Part III, (Bonora and Ruggiero, 2004c), the methodology have been applied to ferritic–perlitic DCI highlighting the competition, between ductile and brittle fracture in the ferritic and perlitic phase respectively, which drives the overall material response and performance.

The present work has been organized as follows: in Section 2 the UCM development is discussed and details of the finite element modeling are given; in Section 3, the constitutive modeling of the constituents is analyzed with particular attention to the graphite nodule response; in Section 4, the damage mechanisms in the DCI mesostructure and the related failure models are discussed; in Section 5, the results of a parametric study finalized to investigate the effects associated to the cooling phase modeling, the cell choice, constituent modeling, and damage induced effects, are given and compared with experimental data available in the literature. Finally, in Section 6, the principal outcomes of this work are summarized in the conclusions.

2. Unit cell model

A number of possible unit cell models can be developed according to the material microstructure. As far as concerns materials with included spherical particles, similarly to Brocks et al. (1996), it is assumed that particles are homogeneously dispersed in the matrix material and the microstructure can be assumed to be periodic of hexagonal micro-cell units, which are approximated by circular cylinder as depicted in Fig. 1. From this, 2D axisymmetric unit cell FEM model can be developed simply meshing half of the cell only, for symmetry reasons.

For the axisymmetric cell, the principal true strains are given, at the mesoscale, by:

$$\begin{aligned} E_{33} &= \ln\left(1+\tfrac{\Delta L}{L_0}\right) \\ E_{22} &= E_{11} = \ln\left(\tfrac{R}{R_0}\right) \end{aligned} \tag{1}$$

where the cell volume change is given as:

$$E_H = \frac{V - V_0}{V_0} = E_{33} + 2E_{22} \tag{2}$$

Similarly, meso-stresses are defined averaging the reaction forces, F_{ij}, along the cell boundary over the deformed cell face areas.

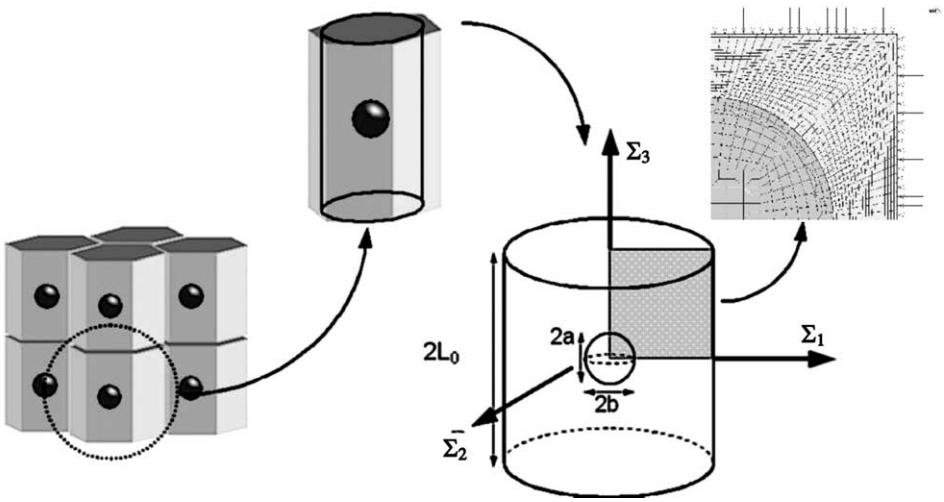

Fig. 1. Microstructure simplification and meso-scale unit cell model definition.

$$\Sigma_{11} = \Sigma_{22} = \frac{F_{11}}{2\pi Rh}$$
$$\Sigma_{33} = \frac{F_{33}}{\pi R^2} = \frac{F_{33}}{\pi[R_0 \exp(E_{11})]^2} \tag{3}$$

The equivalent von Mises stress, together with the hydrostatic pressure and stress triaxiality (triaxiality factor, TF) definitions are given as follows:

$$\Sigma_{eq} = |\Sigma_{33} - \Sigma_{11}|$$
$$P = \frac{2\Sigma_{11} + \Sigma_{33}}{3} \tag{4}$$
$$\mathrm{TF} = \frac{P}{\Sigma_{eq}} = \frac{1}{3} \cdot \frac{2\Sigma_{11} + \Sigma_{33}}{|\Sigma_{33} - \Sigma_{11}|}$$

In the axisymmetric formulation, as well as plane stress, the stress triaxiality expression is independent on the material Poisson ratio.

The UCM has been modeled with finite element method using four node, isoparametric, and arbitrary quadrilateral element written for axisymmetric applications. As this element uses bilinear interpolation functions, the strains tend to be constant throughout the element. The spheroid and the matrix have been simulated as separated deformable bodies. Finer mesh has been used for the matrix material. The reference Cartesian x-axis is the axisymmetry axis (Z) while the y-axis is the radial one (R). Fixed displacement boundary conditions have been applied to the bottom (Z-axis) and left side (R-axis) respectively. Plane-remain-plane conditions have been applied to the top and right side of the cell via tying on the appropriate node degrees of freedom. The master node, at the top right cell corner, is used to apply the prescribed

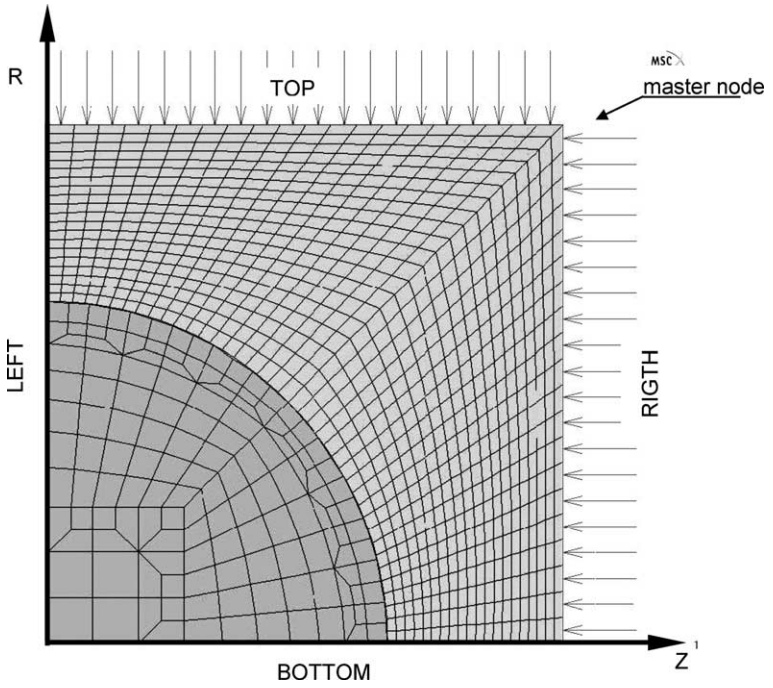

Fig. 2. DCI unit cell finite element mesh.

displacement history and to record the resultant of cell reaction forces. Numerical simulations have been performed with MSC/MARC2003 commercial finite element code. In Fig. 2, the reference finite element mesh for the cell is given. Contact between the matrix and the spheroid may occur along the contact interface. No friction has been considered at this time. No special interface elements or cohesive contact force law has been prescribed. Contact may occur when the distance between nodes belonging to different bodies becomes smaller than a prescribed value. Penalty based algorithms preventing penetration between bodies have been used. Separation between bodies will occur when the separation traction exceeds the maximum reaction force. Elastic plastic analyses have been performed using finite plasticity formulation, as well as large displacement and Lagrangian updating. True stress–true strain at mesoscale has been determined according to Eq. (1), (3) and (4).

3. Constituents thermo-mechanical behavior and modeling

The development of an accurate UCM relies not only on the correct recognition of the material periodic microstructure, but also on the capability to infer the appropriate material constitutive models for both the constituents and phases present in the cell.

Relatively to DCI, as mentioned in the introduction, this issue has been probably oversimplified in the past published works, where the discussion on the effective graphite nodule properties has been, most of the time, avoided asserting that, since graphite spheroids are known to be soft, no contribution is expected from these on the material overall stiffness. This statement is only partially true and, at the same, misleading.

As a matter of fact, graphite spheroid, if considered under the composite material conceptual framework, is a type of reinforcement with negative effect on the overall properties, since it is known that the stress–strain DCI response is of inferior quality than that of the matrix material alone. In addition to this, spheroid hardness is at least half of that of the matrix, justifying the attribute of ''soft'' material.

However, treating the DCI as analogous to a simple voided matrix material is conceptually wrong for the following reasons. Firstly, there are indications that suggests that graphite spheroids are nearly incompressible under hydrostatic pressure and that can exhibit some structural resistance (Steglich et al., 1996). This opposition to compressive state of stress causes local Poisson effects during loading that, in many cases, cannot be neglected. This feature is confirmed by the fact that the DCI stress/strain response is better that that of simply voided matrix. Secondly, it is known that DCI shows different stress–strain response under tension and compression. This feature can be naturally explained, as it will be demonstrated later in the paper, only if the nodule stiffness contribution is taken into account. Finally, the DCI yield strength is directly related to the strength of the interface between the matrix and the spheroid; if the spheroid would have no role the DCI yield strength should be exactly equal to the one of the voided matrix material.

As far as the authors are aware of, detailed information about the effective graphite nodule mechanical behavior is still lacking in the published literature. The reported Young modulus values for the graphite spheroid spread from few thousand of MPa up to 700 GPa that is the modulus of carbon in the diamond form. In most of the cases it is tacitly accepted that nodules are made of graphite having the same mechanical properties as those for bulk macroscopic graphite (IAEA, 1979).

At present, the debate about the real nature of the graphite spheroids and their forming process is still open. Even though many theories have been proposed since 1965, today the more accredited model for the nucleation of graphite spheroids is the so-called ''melt-theory'' (Scheil and Hutter, 1953). On the contrary, the way in which spheroids grow is not completely clear yet. A commonly accepted idea is that the nodule formation occurs by a growing austenite shell. The nodule grows in contact with the melt and is encapsulated by austenite, and further growth of the nodule within the shell takes place by solid-state carbon diffusion. Consequently the nodule growth is assumed to start from the center and to proceed by thickening of

the carbon layers. Alternatively to this, radial structures found in well-polished samples have been showed as "proof" of radial growth mechanism of nodules. In the opposite direction, Karsay and Campomanes (1970) and Stadelmaier (1960), advocating the "bubble theory", proposed that nodule growth starts at the periphery and proceeds towards the centre. Even though these theories diverge, all of them agree on the fact that the resulting nodule structure is a layered system similar to onionskin like arrangement.

Even the graphitic nature of the spheroids, always mentioned in the papers, is not always verified. As a matter of fact, there are clear evidences that the non-graphitic carbon is found in both nodules and flakes. For instance, Purdy and Audier (1984) found amorphous carbon in both nodule, flake and along the borderline graphite–iron. Recently, Zhukov and Ramachandra (1994) reported on new diamond-like allotropic forms of carbon, also found in cast iron. It can therefore be noted that all known carbon structures, ranging from amorphous to diamond, can be found in cast iron depending on the applied cooling conditions. Amorphous carbon is a very hard and strong compound while graphite is softer due to the crystalline order and closer spacing between monoplanes and stacks. Consequently the choice of material mechanical properties to be used in the UCM needs some attentions since large variations are found in the referenced values, according to the carbon type.

In some studies, performed in the 70s on graphite for nuclear applications, bulk graphite elastic–plastic behavior with a tangent modulus approximately half of the Young modulus is also reported, (Tatsuo et al., 1979). In the present work, preliminary finite element investigation showed no relevant effect due to the non-linear behavior; consequently, the spheroid material has been assumed linear elastic. Thermal expansion coefficient reported in the literature shows a variability usually ranging between 0.6 and $4.3 \times 10^{-6}\,\mathrm{K}^{-1}$ and small variation with temperature. Here, it has been taken constant with temperature and equal to $2.5 \times 10^{-6}\,\mathrm{K}^{-1}$. Therefore, the effective Young modulus for the spheroid material has been determined though a parametric finite element analysis looking at the resulting effect on the predicted DCI structural response (stiffness and yield strength) as described later in paper.

The matrix material may have different microstructures according to the cooling rate, carbon content and heat treatment. In this paper, the attention has been limited to the case of pure ferritic matrix, which is known to be ductile and to fail by plastic strain accumulation. The reference DCI material used in this investigation is GGG40, in Table 1 the composition as well as the average reference properties are given. Usually, this material has a well controlled microstructure with an average graphite diameter, d_g, of 55–60 μm, a grain size of 30–60 μm, a mean distance between spheroids, λ, of 50–100 μm and a shape factor, f, not less than 0.84 ($f = 1$, spherical shape).

In the simulation the ferrite has been modeled as elastic–plastic von Mises hardening material. The elastic–plastic response at room temperature for the matrix material is given in Fig. 3 (Zhang et al., 1999). Temperature effect on the Young modulus, yield strength and thermal expansion coefficient has been also taken into account. In Table 2 the variation of each property as a function of temperature is also given. Missing values at different temperatures have been linearly interpolated between upper and lower bounding values.

The ferritic material plastic flow curve at different temperatures has been assumed to be self-similar to the one at room temperature, scaled with respect to the actual yield stress. On the $\ln(\sigma) - \ln(\varepsilon_p)$ plot the plastic flow data show a two-slope behavior characterized by two well defined hardening exponents, as given in Fig. 4.

The knowledge of temperature effect on material properties is fundamental in order to determine the residual stress/strain state which occurs in the material microstructure due to the cooling process from

Table 1
Composition and reference properties for purely ferritic GGG40 DCI

	C [wt.%]	Si [wt.%]	Mn [wt.%]	Cu [wt.%]	$P_{(max)}$ [wt.%]	Tensile strength [MPa]	Yield stress [MPa]	Elongation [%]
GGG40	3.5–4.0	2.3–2.8	0.3 max	–	0.05	420	280	15–22

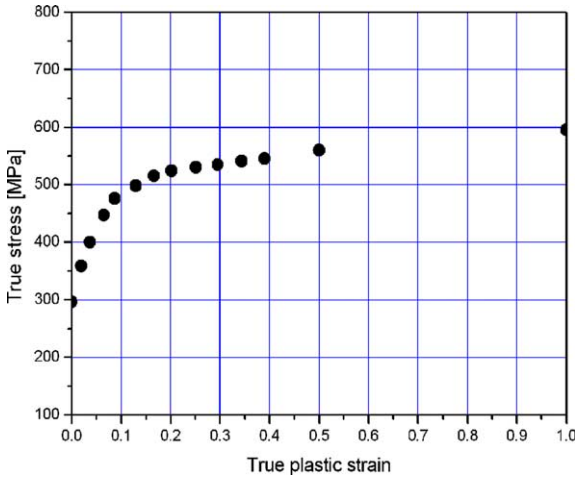

Fig. 3. True stress vs. true plastic strain for ferrite at RT (after Zhang et al., 1999).

Table 2
Material properties for pure ferritic matrix as a function of temperature

Temperature (°C)	Young modulus (GPa)	Thermal exp. coeff. (mm/mm °C)	Yield strength (MPa)
25	210.0	1.25×10^{-5}	297
250	153.8	1.50×10^{-5}	194
500	102.5	1.60×10^{-5}	137
750	41.4	–	96
900	20.0	–	70
1000	0.1	2.40×10^{-5}	60

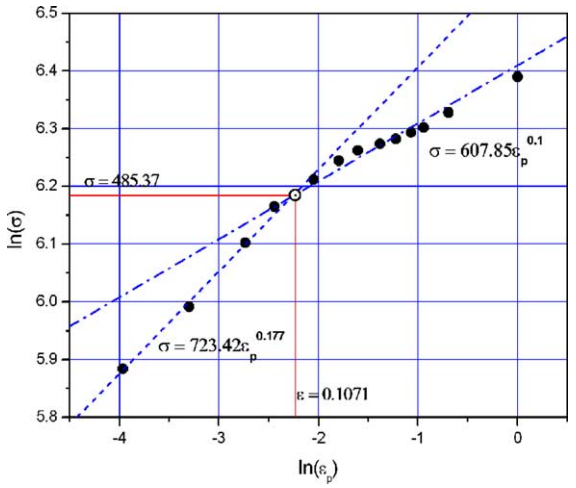

Fig. 4. Two-slope behavior on the ln–ln plot for the plastic flow curve for ferrite at RT.

the liquid to room temperature. According to the melt theory the nodules are already present in the DCI liquid phase. Assuming that the cooling from the liquid state of a well-inoculated iron occurs under equilibrium conditions, the first solid to crystallize in a hypereutectic iron (%C or carbon equivalent, CE = 4.5%) at the liquidus temperature is the graphite phase (point A, Fig. 5b). These graphite nuclei grow until the temperature reaches the eutectic transformation range (point B, Fig. 5b). Below 1147 °C, that is the eutectic solidification lower bound temperature, the DCI is no longer in the liquid state, and the nodule counts does no longer change while nodule dimension may vary due to carbon solid diffusion processes, associated to the transformation of the austenite in ferrite, which theoretically may occur down to the eutectoid reformation temperature. In Fig. 5a, the schematic Fe–C binary diagram is given showing both the major transformation boundaries and the associated phases and microstructures. The right-hand picture shows a close-up of the corresponding region of interests for the cast iron ternary diagram.

As far as the microstructure and the unit cell development are concerned, it can be reasonably assumed that below 1000 °C spheroids are completely formed both in number (i.e. C weight percentage content) and dimensions. Since at this temperature solidification has completely occurred, stress free condition can then be assumed for the elementary cell. Thus, residual stresses at the interface can be simply estimated simulating the cooling phase from 1000° to room temperature. Elastic–viscoplastic behavior of the matrix material, in the temperature range between 500 and 1000 °C, can affect the resulting state of stress at the matrix-spheroid interface. In order to model the associated effects, time dependent material properties, as well as time dependent deformation processes, such as creep, should be part of the analysis. In that case, the determination of the evolution with time of the unit cell boundary conditions becomes a very challenging task. DCI ferritic grades are usually obtained with a two-stage ferritizing annealing process, which also includes austenization at 920–940 °C for 1–4 h; cooling in the furnace to 720–740 °C and soaking at this temperature for 1–4 h; slow cooling in the furnace to 600–620 °C and further cooling in air. This process, as other heat treatments, has the major effect to relief the macroscopic residual stresses (Holden, 1995) resulting from rapid or differentiated cooling in the material, while microscopic residual stress induced by the thermal

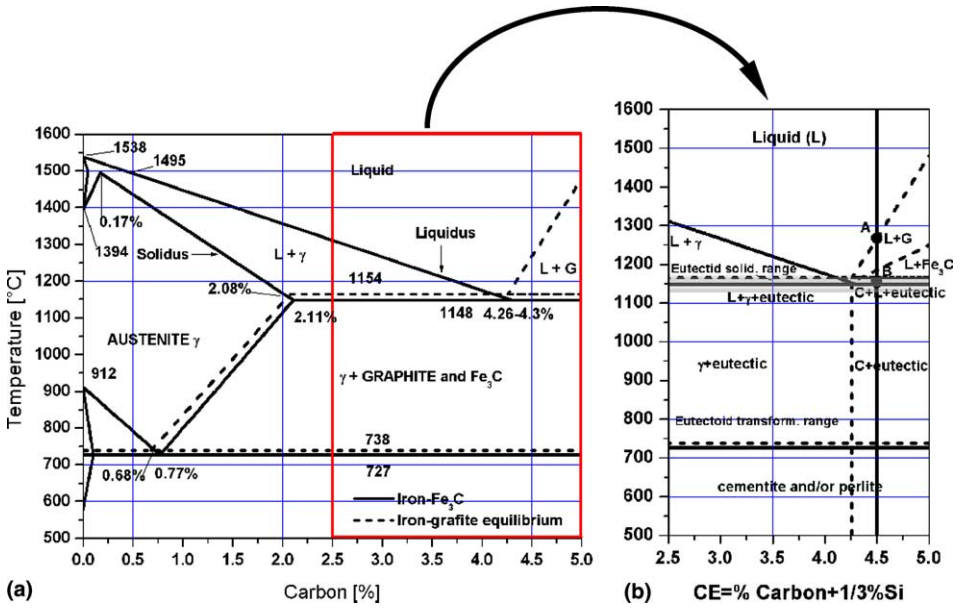

Fig. 5. (a) Schematic Fe–C binary phase diagram and ternary diagram for ductile cast iron. (b) Point A, graphite first solidification; point B, completation of graphite nuclei main growth phase.

expansion coefficient mismatch between the nodule and the matrix remain confined in the microstructure. Recently, Agrawal et al. (2003), investigated the thermal stress distribution in two-phase co-continuous composites using neutron diffraction technique and they found that the residual microstresses distribution around the Al_2O_2 particles can be fairly well predicted using rate independent finite element modeling, simulating the temperature jump from the so-called *effective processing temperature*. Similarly, Ismar et al. (2001), this time using rate dependent material constitutive modeling, found that, at least in continuous fiber reinforced metal matrix composite, the processing cooling rate does not have a robust effect on the resulting macroscopic material stress–strain response, while it is strongly affected by the processing temperature jump and constituent CTE mismatch that drive the onset inelastic yielding during the cooling process. In the present work a time independent approach has been used and the viscous effects associated to a given cooling rate have not been considered. Here, the attention has been focused mainly on the stress states that inevitably result from the thermal coefficient expansion (CTE) mismatch in the two phases.

4. Constituents failure mechanisms and damage modeling

Failure at the macroscale is the resulting action of the evolution of irreversible processes that occur at the material microscale. As far as DCI is concerned, macroscopic failure can be ascribed to the progressive damage of each of its constituent phases. From a mesoscopic point of view, damage can occur as:

- spheroid rupture;
- ductile damage in the ferritic matrix;
- spheroid–matrix debonding

These basic micromechanisms of failure usually take place in the material according to a clear sequence that is controlled by the strain level superimposed on the RVE.

4.1. Spheroid fracture

Fracture mechanics investigation, performed on bulk reactor graphite, confirms the brittle nature of graphite for which fracture instability occurs for fracture toughness values lower than $1.0\,\mathrm{MPa\,m^{1/2}}$. Graphite tensile strength reported in the literature ranges from 20 to 30 MPa for the bulk graphite (measured on smooth round specimen with a diameter 2.5–30 mm) to 1.5–3.0 GPa for graphite fiber (average diameter 7 μm). Consequently, spheroid fracture can be investigated using either a maximum stress fracture criterion or a Weibull stress based probabilistic approach. As far as concerns this latter approach, Brocklehurst and Kelly (1979) found for the probability of failure for bulk graphite, given in the form,

$$p_{\mathrm{f}} = 1 - \exp\left[-\left(\frac{\sigma}{\sigma_0}\right)^m\right] \tag{5}$$

a Weibull exponent of $m = 16$ and a scale stress value of $\sigma_0 = 22\,\mathrm{MPa}$.

4.2. Ductile matrix damage

Damage in the ductile matrix occurs as a result of the accumulation of inelastic deformation. Since the ferritic matrix is ductile, microvoids may nucleate both at the grain boundaries and at the secondary small particle inclusions. The growth of these voids is driven by the level of plastic deformation and the stress triaxiality which is the result of the local multiaxial state of stress, induced by the spheroid stress concentration action, and the overall stress triaxiality eventually induced by geometry changes at the macroscale.

This damage process may be accurately described using continuum damage mechanics (CDM) approach. In 1985 Lemaitre, continuing the early work initially developed by Kachanov, proposed a continuum mechanics conceptual framework for ductile damage in metals. Here, the damage accounts for the resulting detrimental effects, which result from the numerous irreversible processes that occur in the microstructure under straining, on the mesoscopic material constitutive response. Consequently, the approach is not restricted to one single specific process, such as microvoids nucleation and growth, but it accounts for all resulting effects associated to the damage processes (microcrack forming, secondary smaller void nucleation, particle breaking, etc.) and their mutual interaction.

One of the key assumptions of CDM is the existence of damage dissipation potential similarly to plasticity theory. In the last decades, a number of damage models have been proposed in the literature assuming different form for the damage dissipation potential. In most of the cases these models were specific for some class of metals only and limited to simple uniaxial loading only. In 1997 Bonora proposed a new CDM model capable to describe different damage evolution with strain in different classes of metals using a unique damage dissipation potential. The model exhibits a number of important features such as: a limited number of damage parameters each having a clear physical meaning, transferability of the damage parameters from specimen to structure, correct accounting of stress triaxiality effects, the possibility to incorporate strain rate and temperature effect as well as complex load path involving reversal plastic flow.

One of the key difference with respect to other standard CDM formulations is that the effective stress definition does not apply to the material yield function since it is impossible to experimentally separate material hardening and damage softening, consequently the proposed model does not show the localization problems that strongly constrain other formulations involving softening. Much more detailed discussion about this issue can be found elsewhere (Pirondi and Bonora, 2003).

Under the assumption of isotropic damage and isotropic hardening material, the set of constitutive equations for the damaged material can be summarized as follows:

(a) the plastic and damage dissipation potentials are written as,

$$\varphi = F_{\mathrm{p}}(\sigma, K; D) + F_{\mathrm{D}}(Y; p, D) = [\sigma_{\mathrm{eq}} - f(K; D)] + F_{\mathrm{D}}(Y; p, D) = 0 \tag{6}$$

where $f(R;D)$ is the macroscopic material plastic flow and F_{D} is the damage dissipation potential defined as,

$$F_{\mathrm{D}} = \left[\frac{1}{2}\left(-\frac{Y}{S_0}\right)^2 \cdot \frac{S_0}{1-D}\right] \cdot \frac{(D_{\mathrm{cr}} - D)^{\frac{\alpha-1}{\alpha}}}{p^{\frac{2+n}{n}}} \tag{7}$$

(b) total strain tensor decomposition,

$$\varepsilon_{ij}^{\mathrm{T}} = \varepsilon_{ij}^{\mathrm{e}} + \varepsilon_{ij}^{\mathrm{p}} \tag{8}$$

(c) elastic strain tensor,

$$\varepsilon_{ij}^{\mathrm{e}} = \frac{1+\nu}{E}\frac{\sigma_{ij}}{1-D} - \frac{\nu}{E}\frac{\sigma_{kk}}{1-D}\delta_{ij} \tag{9}$$

(d) total equivalent plastic strain rate tensor,

$$\dot{\varepsilon}_{ij}^{\mathrm{p}} = \dot{\lambda}\frac{\partial F_{\mathrm{p}}}{\partial \sigma_{ij}} = \dot{\lambda}\frac{3}{2}\frac{\dot{s}_{ij}}{\sigma_{\mathrm{eq}}} \tag{10}$$

(e) plastic hardening rate (plastic multiplier),

$$\dot{\kappa} = -\dot{\lambda}\frac{\partial F_{\mathrm{p}}}{\partial K} = \dot{\lambda} = \dot{p} \tag{11}$$

Eqs. (10) and (11) are those for standard plasticity while the kinetic law of damage evolution is given by:

$$\dot{D}^{+} = -\dot{\lambda}\frac{\partial F_{\mathrm{D}}}{\partial Y} = \alpha \cdot \frac{(D_{\mathrm{cr}} - D_0)^{\frac{1}{\alpha}}}{\ln(\varepsilon_{\mathrm{f}}/\varepsilon_{\mathrm{th}})} \cdot f\left(\frac{\sigma_{\mathrm{m}}}{\sigma_{\mathrm{eq}}}\right) \cdot (D_{\mathrm{cr}} - D^{+})^{\frac{\alpha-1}{\alpha}} \cdot \frac{\dot{p}^{+}}{p^{+}} \tag{12}$$

with

$$f\left(\frac{P}{\sigma_{\mathrm{eq}}}\right) = \frac{2}{3}(1+v) + 3 \cdot (1-2v) \cdot \left(\frac{P}{\sigma_{\mathrm{eq}}}\right)^{2} \tag{13}$$

that accounts for stress triaxiality

$$\dot{p}^{+} = \dot{\lambda} \cdot H\langle f(\sigma_{\mathrm{m}}/\sigma_{\mathrm{eq}})\rangle \tag{14}$$

is the active equivalent plastic strain that accumulates in tension only, while the effective active modulus is given by,

$$\tilde{E} = E(1 - D^{+}H\langle f(\sigma_{\mathrm{m}}/\sigma_{\mathrm{eq}})\rangle) \tag{15}$$

$$H\langle f(\sigma_{\mathrm{m}}/\sigma_{\mathrm{eq}})\rangle = \begin{cases} 0 & \sigma_{\mathrm{m}}/\sigma_{\mathrm{eq}} < 0 \\ 1 & \sigma_{\mathrm{m}}/\sigma_{\mathrm{eq}} \geqslant 0 \end{cases} \tag{16}$$

The formulation requires the identification of the following four damage parameters: $\varepsilon_{\mathrm{th}}$, that is the damage threshold strain at which damage processes initiate; ε_{f}, that is the theoretical strain to failure under constant triaxiality (TF = 0.333); D_{cr} is the critical damage at which complete failure occurs and α is the damage exponent that defines the shape of damage evolution curve with strain. These parameters can be easily identified in uniaxial tensile test as discussed in Bonora (1999).

As far as concerns the present investigation, damage parameters for the ferrite matrix have been taken equal to those for ARMCO iron (Bonora and Milella, 2002) and given in Table 3.

4.3. Matrix–spheroid debonding

Debonding between the matrix and the included spheroid occurs when the applied stress overcomes the residual stress at the interface resulting from the cooling process. The easiest way to account for this damage mechanism in the simulations is to model the cooling phase. This approach will not require any arbitrary interface strength model. The strength of the interface is mainly function of the thermal expansion coefficient mismatch and almost insensitive to the relative difference in the matrix–spheroid stiffness. From the damage point of view the complete particle debonding is analogous to sudden activation of an initial porosity in the matrix material constitutive response. In the literature, DCIs have been modeled as porous solid, which behaves as Gurson-like material. Here, material failure is caused by the growth and coalescence of these initial mesovoids. Conversely, there are clear experimental evidences that DCI failure is caused by the development of ductile damage in the matrix material that fails by smaller microvoids nucleation and growth underling the need to account for this mechanism, (Liu et al., 2002). Thus, the possibility to correctly account for the debonding process is critical in the accurate prediction of both macroscopic DCI yield strength and the slope of the hardening tangent modulus.

Table 3
Damage parameters for ferrite

$\varepsilon_{\mathrm{th}}$	ε_{f}	D_{cr}	α
0.0037	0.5	0.45	0.3

5. Numerical results

The UCM described in the previous section has been used to investigate a number of aspects related to the nature of the contact between the spheroid and the matrix, the spheroid stiffness, the role of stress history resulting from the cooling down to RT and damage induced effects.

Finite element results have been compared with experimental data available in the literature for a GGG40 DCI. Experimental stress–strain data reported by Kohout (2001), Berdin et al. (2001) and Zhang et al. (1999) for the same DCI have been collected showing a very good agreement and limited experimental scatter. Since at large strain the DCI response is dominated by the ferrite behavior, data in the early near yield regime are needed in order to appreciate the differences in the constituents modeling. To this purpose, the experimental work performed by Kohout (2001) is of particular interest since stress–strain data in the strain range below 0.1% are given.

5.1. Matrix–spheroid bonding and residual stresses effect

Firstly, the effective role played by the cooling down process has been verified. In Fig. 6, the stress–strain response, obtained with the UCM without the simulation of the cooling phase (that means stress free at RT condition) is given for two choices of the graphite Young modulus (E_g) and compared with the experimental data. The stress free condition at RT makes the UCM response independent of the graphite Young modulus, since the spheroid is practically completely debonded. The only expected difference is in the lateral contraction during uniaxial loading. As shown in Fig. 6, the difference in stress of the two calculates stress–strain curve is merely appreciable and less than 3% in stress. The comparison with the experimental data shows substantial differences in the linear stress–strain range, a higher predicted modulus, and lower than measured yield strength.

Kohout (2001) pointed out the impossibility to define a unique Young modulus for DCI due to almost continuous variation of the stress–strain slope even though in the early deformation range (<0.05%). At the same time, he highlighted the difficulty to conventionally define a yield strength for the cast iron and ascribed this non-linear behavior to the stress concentration induced by the spheroid-void shape. Conversely, simulation of stress free at RT UCM, or alternatively voided matrix UCM, shows only a well defined linear

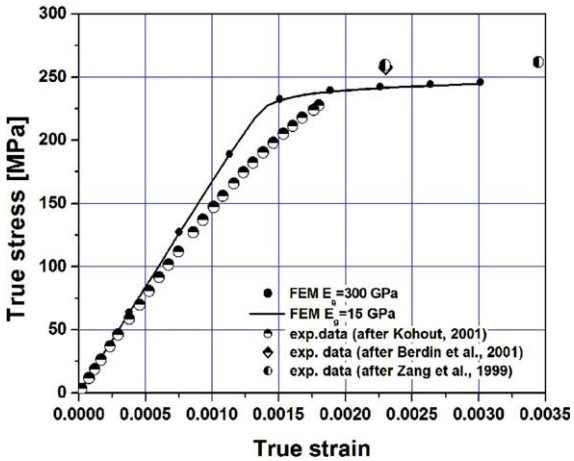

Fig. 6. Comparison of the UCM response and experimental data for GGG40: FEM response is given for two graphite modulus values (15 and 300 GPa) in the case of stress free at RT (no residual stresses resulting from the cooling down phase).

trend in the stress–strain response with a Young modulus of 167 GPa ± 0.0195 (standard error), with a correlation coefficient $R = 0.9997$ and a standard deviation $SD = 0.526$, that is in agreement with the theoretical upper bound value of 170 GPa obtained for a cylindrical cell with a spherical void.

The role of the residual stresses and the bond type on the overall stress–strain response is given in Fig. 7. Here, three reference cases have been investigated and compared: (a) simple voided matrix (no spheroid), (b) perfectly matrix bonded spheroid (no debonding is allowed), (c) spheroid bonded to the matrix by the residual stress. In all three cases the cooling phase has been simulated. The two extreme cases, case A and B, show almost the same stiffness. This is mainly due to the fact that in case B, the residual stresses are frozen in the cell but cannot activate any debonding process. In case A, the residual stresses are zero since the simple voided cell can contract freely. The difference in the resulting yield stress is clearly due to the graphite stiffness and the induced stress triaxiality for the case B. On the contrary, case C shows lower stiffness and yield strength. Here, the non-linearity in the elastic range response starts to be visible. In Fig. 8, the calcu-

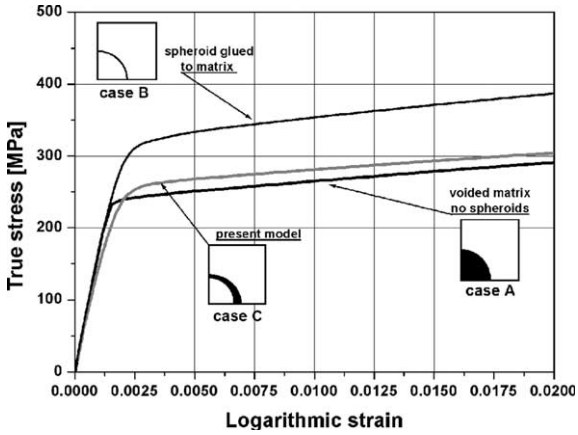

Fig. 7. Matrix–spheroid bonding effect: all cases account for the cooling down to RT phase. In case B, glued, no debonding can occur during the entire deformation process.

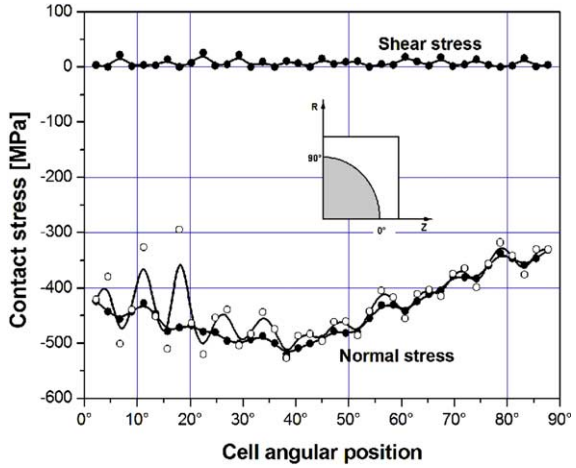

Fig. 8. Residual stress distribution along the contact interface at the end of the cooling phase (i.e. RT). The comparison is given for two graphite stiffness values: full symbol, 375 GPa; hollow symbol, 100 GPa.

lated angular distribution of the normal and shear stress component along the contact interface, at RT, is also given, for two graphite Young's modulus values, showing a zero shear and almost uniform compression state of stress with a maximum around 40°–45°, approximately. Here, the amplitude of the normal contact stress at the interface seems to be independent from the graphite stiffness for values sufficiently high to oppose some resistance to the matrix thermal contraction. From a computational point of view, the normal stress along the interface becomes more and more oscillating, with an upper bound value close to 500 MPa approximately, as the graphite stiffness is progressively reduced. This behavior is an intrinsic characteristic of the penalty method used in the contact algorithm involving deformable–deformable body contact. Consequently, these values for the residual contact stresses should be taken as indicative. If an average reference value is taken from the oscillating distribution, numerical simulations show that the magnitude of the normal contact stress rapidly increases from 0 to 500 MPa approximately, for graphite stiffness values ranging from 0 to 50 GPa. Further increases of the graphite stiffness do not result in an increase of the contact stress that seems to reach a saturation value. On the contrary the oscillating feature of the contact stress distribution becomes less pronounced. The oscillating distribution of the residual stresses at the contact interface does not have any appreciable effect on the debonding process that occurs much later in the deformation process when the unit cell has gone under extensive plastic deformation and local stress redistribution. Since the node separation along the contact interface occurs when the local normal stress exceed the reaction force on the node in contact, this reference value is averaged on the elements of both bodies insisting on the same node and, consequently, the eventual effects due to an oscillating feature of the contact stress distribution are intrinsically smoothed.

5.2. Graphite stiffness effect

A parametric investigation on the overall UCM response varying the spheroid stiffness and incorporating the cooling down phase has been performed. In Fig. 9 the comparison of the stress–strain response for $E_g = 15$, 150 and 450 GPa is given. With the decrease of the graphite stiffness also the overall stiffness is reduced as well as the reference yield stress at the 0.2% strain offset. It is important to observe that in the strain range below the conventional value of 0.002, the stress–strain curve is not linear. A two-slope behavior becomes more evident for low graphite stiffness values (i.e., 15 GPa). Here, it is worth to be noted

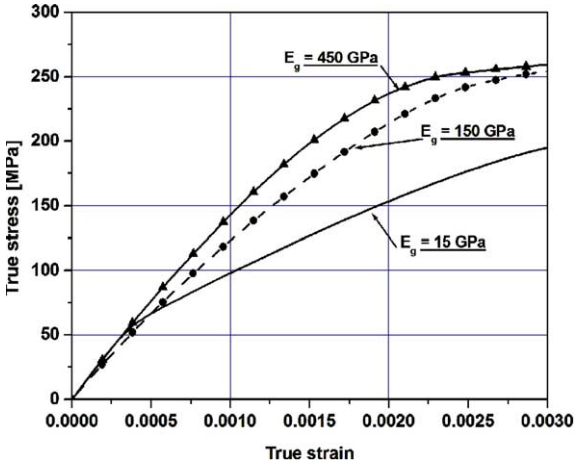

Fig. 9. Graphite stiffness effect on the predicted DCI stress–strain curve incorporating the cooling phase.

that the initial slope, for strain values lower that 0.05%, is slightly steeper than that found for intermediate graphite stiffness values (i.e., 100–150 GPa).

In order to investigate this feature, the predicted DCI initial local tangent ($\partial\sigma/\partial\varepsilon$) variation with the graphite stiffness has been investigated. In Fig. 10, the two slope behavior for $E_g = 90$ GPa is clearly visible (hollow symbols). Here, the linear fit gives an initial DCI stiffness $E = 144$ GPa that drop down to 90 GPa at 20 MPa ($\varepsilon = 0.015\%$) approximately. In the same plot, the evolution of the slope break point, at which the first slope change occurs, is also given (black dots) together with the associated graphite stiffness. It is interesting to observe that increasing the graphite stiffness the first yield stress is reduced with a minimum at 10 MPa ($\varepsilon = 8.0 \times 10^{-5}$) approximately for $E_g = 40$ GPa. For further increases of the graphite stiffness, the first yield stress jump up to values in the range 40 MPa ($\varepsilon = 3.0 \times 10^{-4}$). In Fig. 11, the evolution of the initial (first slope) and the dominant (second slope) DCI stiffness as a function of the graphite Young modulus is given. Here, the predicted initial DCI modulus drops from the upper bound value of 167.8 GPa, specific of the simple voided matrix (no spheroid), down to a minimum value of 117 GPa for $E_g = 45$ GPa. Increasing the graphite spheroid Young modulus the resulting DCI stiffness increases again reaching the upper bound value for $E_g = 1000$ GPa, approximately. Similarly, the DCI dominant stress–strain slope has a sharp drop down to 60 GPa for E_g below 15 GPa, while for higher graphite stiffness values it increases again. This plot indicates that there are potentially two values of the graphite Young modulus for which the resulting predicted DCI stiffness is the same. GGG40 ductile cast iron has a very well controlled microstructure and shows stiffness in the range of 148–155 GPa. For these values, the two possible graphite Young moduli are: 5–30 GPa and 300–375 GPa. The lower stiffness value has to be excluded since the expected DCI stiffness is observed for an initial limited strain range and then drops to lower values as given in Fig. 12, where the comparison with the experimental data is given. This latter result confirms that the graphite nodules have to have a stiffness value of the order of 300–375 GPa. These values may be apparently in contrast with the DCI nodule Young modulus measurements, in range of 15 ± 5 GPa obtained by Dierickx et al. (1996) using nano-hardness indentation test. These low values can be explained taking into account that indentation is performed on cut nodules that, as a consequence of the onion like structure mentioned above, would offer scarce resistance to the peeling action of the indenter.

In summary, if the residual stresses resulting from the jump in temperature from 1000 °C, approximately, down to the RT, are accounted for in the numerical simulation of the unit cell, the DCI predicted stress–strain curve is nonlinear even at very low strain values, as confirmed by the experimental found in Kohout

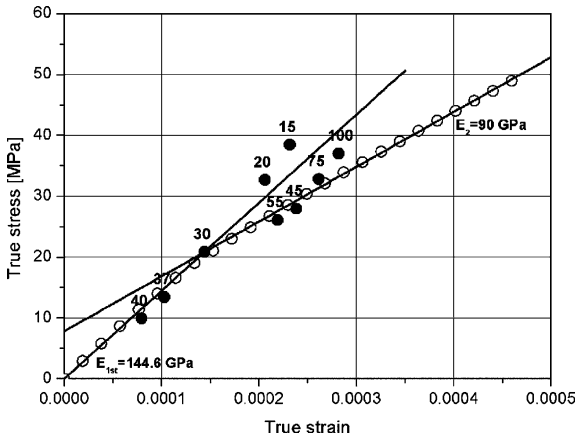

Fig. 10. Two-slope behavior in the early DCI stress–strain curve: hollow symbols, $E_g = 30$ GPa; solids symbols, show the evolution of the slope break point (here indicated as initial yield strength) as a function of the graphite Young modulus.

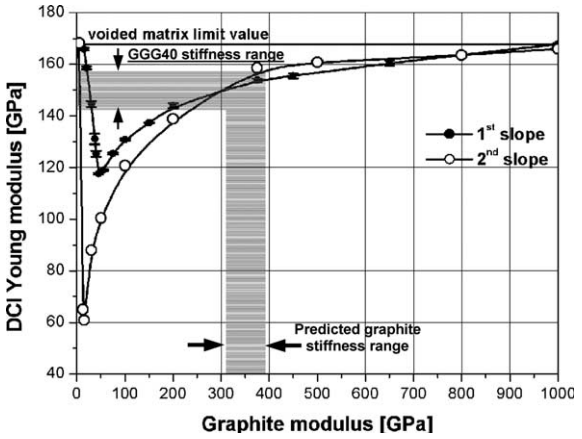

Fig. 11. Predicted initial DCI Young modulus as a function of the graphite stiffness.

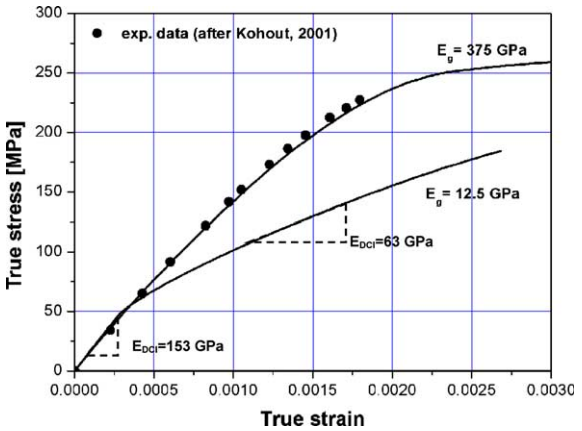

Fig. 12. Comparison of the stress–strain curve, predicted for the two values of E_g and the experimental data.

(2001). At very low strain, the two-slopes behavior of the DCI stress–strain curve becomes much more visible for low E_g values. In the authors opinion, this two-slope behavior of the stress–strain curve, as well as an higher initial tangent modulus for lower E_g values, cannot be attributed to the oscillatory distribution of the normal contact stress at the interface that only increases in value, but not varies in shape, during the loading. Similarly, it has nothing to do with the occurrence of the debonding process that, even at low E_g values, usually occurs much later in the deformation process.

On the contrary, this behavior can be addressed to the different extension of the plastic strain shell that develops, as a result of the cooling stage, around the spheroid. For low E_g values (i.e. $E_g \cong 15$ GPa) the plastic strain is distributed along a thin layer, 25% of the spheroid radius thick approximately. Increasing E_g, the plastic strain develops in form of a diagonal band, as depicted in Fig. 13, frame A. For $E_g > 50$ GPa, the plastic strain distribution does not longer increase in size but only slightly in its spatial gradient and this is in accordance to the fact that for $E_g > 50$ GPa the magnitude of the residual stresses at the contact interfaces do not longer increase with increasing values of E_g. The presence of different plastic volumes modifies the cell overall stiffness and, consequently, the resulting stress–strain curve predicted for the material.

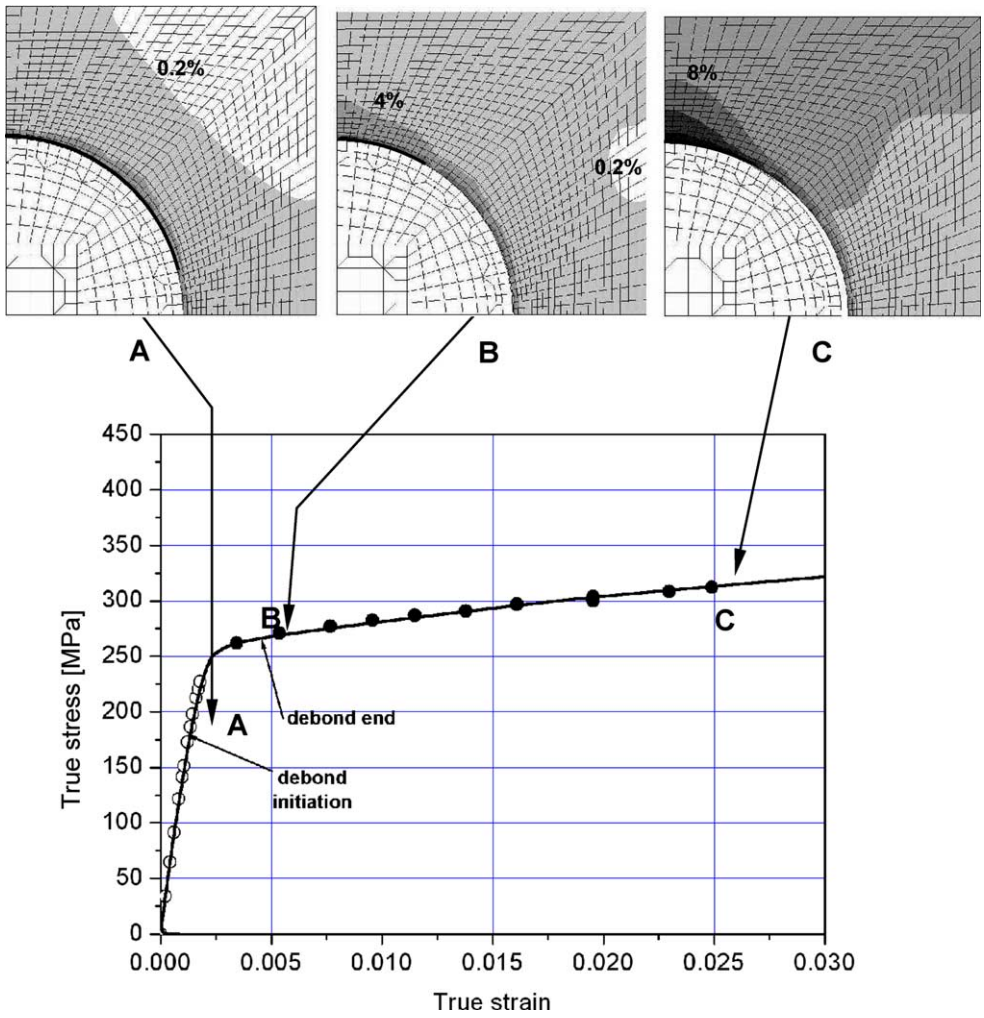

Fig. 13. Comparison of the predicted true stress vs. true strain response and the experimental data (black and hollow dots). Frames A–C show the evolution of the plastic strain and the debonding process with increasing overall cell strain. The load acts horizontally with respect to the showed cell.

Confirmation of the effective presence of a plastic strain distribution around the spheroid and its extension could be experimentally verified by etching techniques.

5.3. Damage modeling

Damage effect and development have been investigated looking at both debonding and ductile damage in the ferrite matrix. As stated in the previous section, two main damage mechanisms take place in the DCI microstructure under straining. Firstly, nodule debonding from the matrix occurs as soon as the applied external load is strong enough to recover the compressive residual state of stress along the interface. Numerical investigation shows that, at the end of the cooling down phase, a shell of yielded matrix material surrounds the nodule, as given in Fig. 13 frame A. The debonding starts to occur well before reaching of the

macroscopic DCI yield strength, at 0.25% approximately (Fig. 13, point A), and it ends immediately after the overcoming of the yield stress at about 0.5% (Fig. 13, point B). From this point ahead, the DCI can be conceptually considered as a voided matrix material with an initial porosity equal to the graphite nodule volume content. In fact, if a partial unloading is performed at 0.005 strain, the measured Young modulus found is 166.6 GPa that is very close, less that a 1 GPa in difference, to the that for the voided matrix material. It is worth to underline here that even if fully debonded, the spheroids still oppose to the lateral contraction of the cell due to Poisson effect. In Fig. 13, the predicted stress–strain response for the DCI is given in the strain range up to 0.03 together with the experimental data provided by Kohout (2001) and Berdin et al. (2001). Here the evolution of plastic strain in the cell is given for the initial spheroid debonding, at the completion of the debonding process and at 0.025 meso-strain. In this latter situation the matrix of the cell has fully yielded, and the growth of spheroid nucleated void starts to become clearly visible. Together with this damage mechanism, ductile damage in the matrix material starts to develop as soon as plastic deformation initiates to accumulate in the cell. In Fig. 14, the predicted stress–strain curve up to failure is given together with the experimental data. In addition, the damage maps calculated at various strain levels are

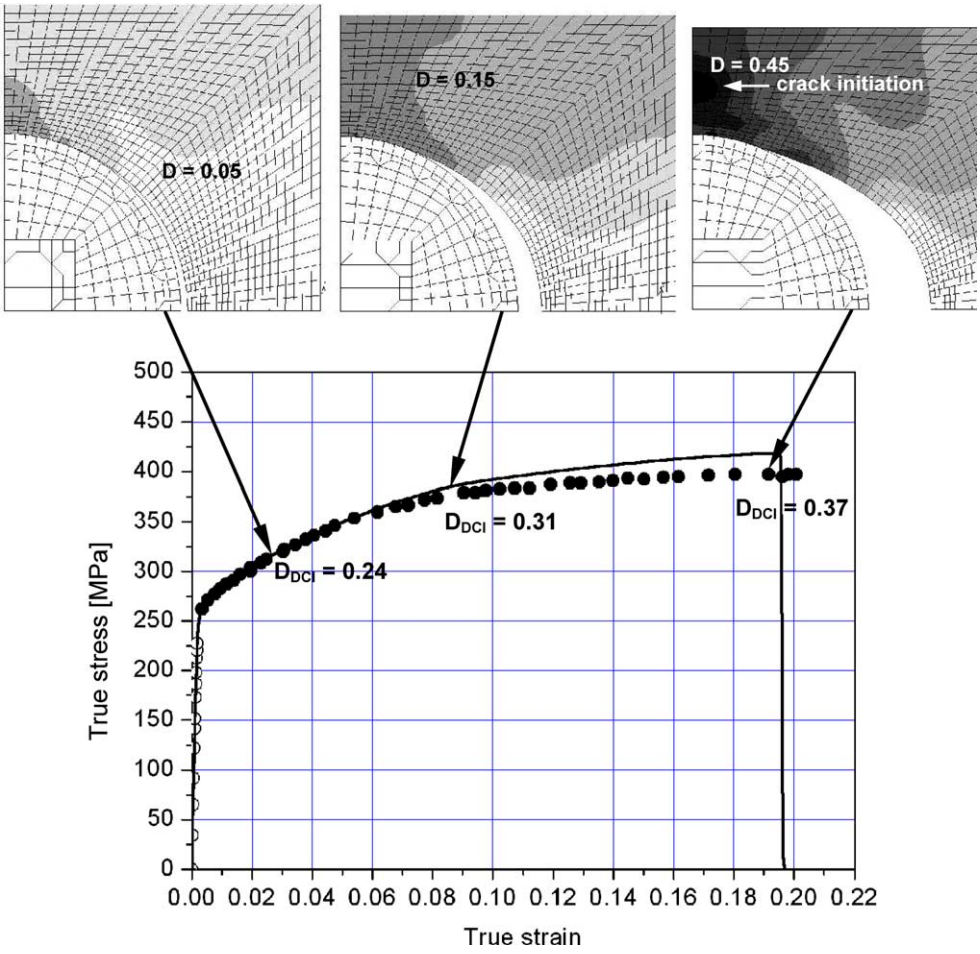

Fig. 14. Comparison of the predicted stress–strain curve up to failure: damage evolution in the cell at different strain levels. The load acts horizontally with respect to the showed cell.

also given and related to the damage observed at the macroscale, D_{DCI}, as stiffness reduction of the DCI. The presence of macrovoids nucleated from spheroids is the driving mechanism for the development of ductile damage into the matrix. Here, the competition of plastic strain and local stress triaxiality determines the condition for the initiation of a ductile crack, as a result of smaller voids nucleation and growth as shown in Berdin et al. (2001), which causes the catastrophic failure in the material.

The comparison given in Fig. 14 shows the good agreement of the predicted response and the experimental data from a global point of view confirming that the damage model is capable to correctly predict the onset failure. In order to have additional verification of the damage model performance, the resulting damage effect, in term of Young modulus reduction at the cell level, has been compared with stiffness loss measurements available in the literature for GGG40 DCI. To this purpose a number of partial unloading has been simulated with the UCM in order to monitor the overall resulting stiffness loss with the increasing

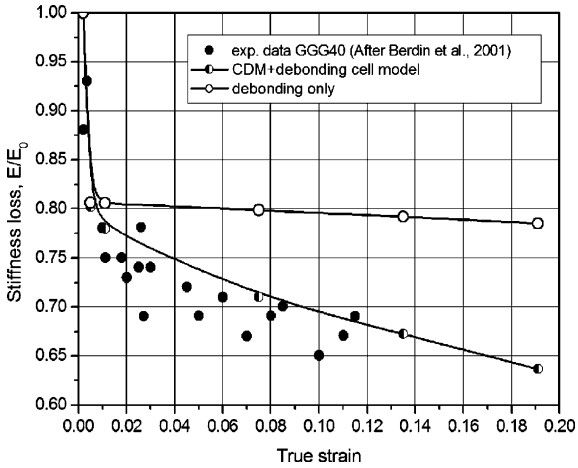

Fig. 15. Stiffness loss evolution in GGG40 DCI: comparison between the experimental data and the present damage model. Hollow symbols indicate predicted damage due to the spheroid debonding only.

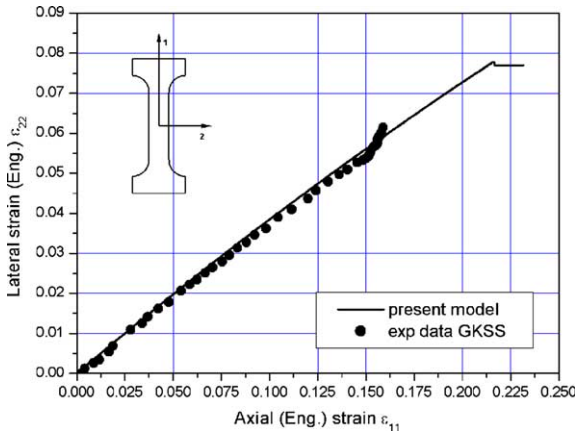

Fig. 16. Comparison of the predicted lateral contraction in a tensile test using the proposed UCM and experimental data (Steglich et al., 1996).

strain level. In order to have an additional confirmation of the role of the damage developed in the matrix material, the same procedure has been repeated in the case of debonding damage only. In Fig. 15 the comparison with experimental damage measurement is given. Probably the major outcome of this damage investigation is that, according to the present results, the growth of macrovoids nucleated at the spheroids is not sufficient to explain failure in DCI. As a matter of fact, it is true that these macrocavities are the first to be generated in the material at very low superimposed strain levels but they can only have a limited growth, which in turns results in a overall damage that practically remains almost constant for further increase of strain. This is also confirmed experimentally by Liu et al. who observed in failed samples only a limited growth of the macrovoids, without coalescence, surrounded by a high density of smaller voids in the matrix material among the spheroids. Thus, the damage in the matrix seems to be the main cause for the

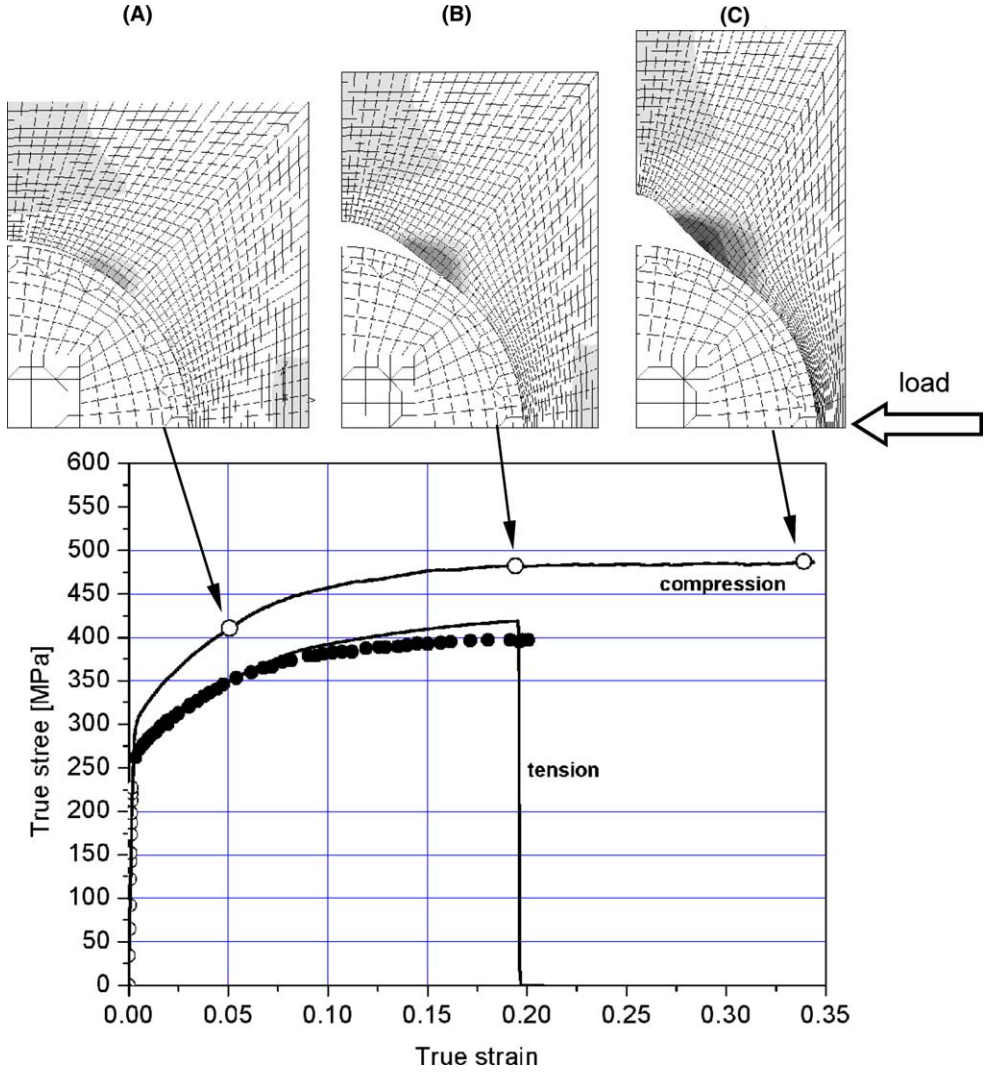

Fig. 17. DCI predicted constitutive response under compression: comparison with tensile response. Frames A–C show damage evolution in the cell for different compressive strain levels. The load acts horizontally with respect to the showed cell.

additional stiffness loss observed in DCI. The comparison given in Fig. 15 shows how the present approach, even though with some uncertainties on the effective ferrite damage parameters, is capable to provide a reasonable upper bound for the expected damage evolution in the DCI. It has to be underlined that the experimental scattered band given in Fig. 15 is also the result of other effects, such as spheroid shape irregularities and clustering which directly influence the local stress triaxiality that is critical for evolution of damage accumulation rate and that has not been incorporated in the present work. An additional verification of the performance of the proposed approach is given in Fig. 16 where the lateral strain, due to Poisson effect, is given as a function of the applied axial strain together with the experimental data measured by Steglich et al. (1996). Once again, the prediction is in a very good agreement with the experimental data. The differences in the strain to failure are mainly due to the elliptical shape of the nodules ($S_f = 0.85$) in the GGG40 DCI tested: the ellipticity is responsible for a higher local stress triaxiality that reduces the potential material ductility. Finally, the DCI constitutive behavior under compressive state of stress has been also investigated. In Fig. 17 the comparison of the predicted material response under both tension and compression is given. Here, $E_g = 375\,\text{GPa}$ has been used and damage modeling has been incorporated in both cases. It is interesting to note that with the proposed approach a higher yield strength in compression than in tension is predicted in accordance with experimental evidences. Here, for most of the spanned deformation range, damage is limited to the debonding of the spheroid from the matrix that is delayed with respect to the tension case and occurs along the cell radial direction. Only later in the compression process, ductile damage in the matrix, that according to the damage formulation used here can only accumulate under positive stress triaxiality conditions, starts to develop at the matrix–spheroid interface along the cell diagonal as given in the frames A, B and C of Fig. 17.

6. Conclusions

In this paper a micromechanics approach has been used to investigate ferritic DCI. The proposed approach has two main features: (a) the residual stresses are accounted by simulating the cooling down stage; (b) main driving damage mechanisms in the microstructure are identified and incorporated in the simulations. In addition to other similar works, here the effective role played by the spheroids on the resulting stress–strain curve has been pointed out. The parametric study performed allowed to determine an indirect procedure for measuring the effective properties of the graphite nodules, that from micro and nanohardness tests are known to be soft but due to their microstructure are practically incompressible under hydrostatic state of stress. The fact that the residual stresses in the cell are calculated by reproducing the cooling down phase allows one to avoid providing arbitrarily matrix–nodule interface strength and to accurately predict damage development as a result of the growth of cavities nucleated from debonded spheroid. The present investigation demonstrated how the damage in the matrix due to plastic strain accumulation, under the action of the external applied load and local geometry drive stress triaxiality, is critical to correctly predict not only global features such as the macroscopic strain to failure but also the evolution of the stiffness loss in the material at mesoscale. This promising approach can be used to investigate other effects such as matrix constituents, multiaxial loading, spheroid ellipticity, etc. and used as tools for multiscale modeling approach.

References

Agrawal, P., Conlon, K., Bowman, K.J., Sun, C.T., Cichocki, J.R., Trumble, K.P., 2003. Thermal residual stresses in co-continuous composites. Acta Materialia 51, 1143–1156.

Aboudi, J., 1989. Micromechanical analysis of composite by the method of cells. App. Mech. Rev. 42 (7), 193–221.

Adams, D.F., Crane, D.A., 1984. Finite element micromechanical analysis of a unidirectional composite including longitudinal shear loading. Computer and Structures 18 (11), 63–65.

Allen, D.H., Boyd, J.G., 1993. Convergence rates for computational predictions of stiffness loss in metal matrix composites. Composite Materials and Structures AMD-Vol. 179/AD-Vol. 37, 31–45.

Berdin, C., Haušild, P., 2002. Damage mechanisms and local approach to fracture, transferability of fracture mechanical characteristics. In: Dlouhý, I. (Ed.). Kluwer Academic Publisher, Netherlands.

Bonora, N., 1997. A Non-linear CDM model for ductile failure. Engineering Fracture Mechanics 58 (1/2), 11–28.

Bonora, N., 1999. Identification and measurement of ductile damage parameters. Journal of Strain Analysis 34 (6), 463–478.

Bonora, N., Milella, P.P., 2002. Simulation of ductile failure in metals under dynamic loading conditions using advanced material damage modeling. Interim Report no. 3, AFRL/EOARD F61775-01-C0003.

Bonora, N., Ruggiero, A., 2004a. Micromechanical modeling of composites with mechanical interface. Part I: Unit cell model development and manufacturing process effects. Composites Science and Technology, in press.

Bonora, N., Ruggiero, A., 2004b. Micromechanical modeling of ductile cast iron incorporating damage. Part II: Pearlitic ductile cast iron. International Journal of Solids and Structures, submitted.

Bonora, N., Ruggiero, A., 2004c. Micromechanical modeling of ductile cast iron incorporating damage. Part III: ferritic–pearlitic ductile cast iron. International Journal of Solids and Structures, submitted.

Bonora, N., Marchetti, M., Costanzi, M., Newaz, G., 1994. Micro-damage effects on the overall response of long fibre metal matrix composites. Composites 25 (n.7), 575–582.

Brocklehurst, J.E., Kelly, B.T., 1979. Graphite structure and its relationship to mechanical design. In: Proceedings of IAEA Specialists Meeting, on Mechanical Behavior of Graphite for High temperature Reactors, Gif sur Yvette, France, pp. 42–50.

Brocks, W., Hao, S., Steglich, D., 1996. Micromechanical modeling of the damage and toughness of nodular cast iron materials. Journal de Physique IV 6 (C6), 43–52.

Berdin, C., Dong, M.J., Prioul, C., 2001. Local approach of damage and fracture toughness for nodular cast iron. Engineering Fracture Mechanics 68, 1107–1117.

Dierickx, P., Verdu, C., Reynaud, A., Fougeres, R., 1996. A study of physico-chemical mechanisms responsible for damage of heat-treated and as-cast ferritic spheroidal graphite cast irons. Scripta Materialia 34, 2.

Hashin, Z., Rosen, B.W., 1964. The elastic moduli of fiber-reinforced materials. ASME Journal of Applied Mechanics 31, 223–232.

Hashin, Z., Shtrikman, S., 1963. A variational approach to the theory of elastic behaviour of multiphase materials. Journal of Mechanics and Physics of Solids 11, 127–140.

Holden, T.M., 1995. The determination of macrostresses (type-I stresses) and microstresses (type-II stresses) by neutron diffraction. Proceedings of Material Research Society, MRS 376, 385–390.

IAEA, 1979. International Atomic Energy Agency. In: Patarin, L. (Ed.), Specialists Meeting on Mechanical Behaviour of Graphite for HTRs Summary Report, Fig-sur-Yvette, 11–13 June, France.

Ismar, H., Schöter, F., Streicher, F., 2001. Effect of interfacial debonding on transverse loading behavior of continuous fiber-reinforced metal matrix composites. Computer and Structures 79, 1713–1722.

Jenkins, L., 1984. Ductile iron: an engineering asset. In: Proceedings of the First International Conference on Austempered Ductile Iron. American Society for Metals.

Karsay, S.I., Campomanes, E., 1970. Control of graphite structure in heavy ductile iron castings. AFS Transactions 78, 85/92.

Kohout, J., 2001. A simple relation for deviation of gray and nodular cast irons from Hook's law. Materials Science and Engineering A 313, 16–23.

Labrecque, C., Cagné, M., 1998. Review ductile iron: fifty years of continuous development. Canadian Metallurgical Quarterly 37 (n. 5), 343–378.

Lemaitre, J., 1985. A continuum damage mechanics model for ductile fracture. Journal of Engineering Material Technology 107, 83–89.

Liu, J.H., Hao, X.Y., Li, G.L., Liu, G.Sh., 2002. Microvoid evaluation of ferrite ductile iron under strain. Material Letters 56, 748–755.

Pirondi, A., Bonora, N., 2003. Modeling ductile damage under fully reversed cycling. Computational Material Science 26, 129–141.

Purdy, G.R., Audier, M., 1984. Electron microscopical observations of graphite in cast irons. The Physical Metallurgy of Cast Iron. In: Fredriksson, H., Hillert, M., Uitgave, M. (Eds.), Proceedings of the Third International Symposium on the Physical Metallurgy of Cast Iron, Stockholm, Sweden, August 29–31. North-Holland, New York–Amsterdam, Oxford.

Scheil, E., Hutter, L., 1953. Untersuchungen über die Kristallisation des Gusseisens mit Kugelgraphit. Archiv für das Eisenhüttenwesen (May/June), 237–246.

Stadelmaier, H., 1960. Über Sphärolithenbildung in Metallschmelzen. Z. Metallkunde Heft 10, 601–604.

Steglich, D., Hao, S., Brocks, W., 1996. Micromechanical modelling of the damage and toughness behaviour of nodular cast of iron materials. Proceeding EUROMECH-MECAMAT'96.

Sun, C.T., Vaidya, R.S., 1996. Prediction of composite properties from a representative volume element. Composite Science and Technology 56, 171–179.

Tatsuo, O., Notokuni, E., Taketoshi, A., 1979. Strength and fatigue properties of near isotropic graphite. In: Proceedings of IAEA Specialists Meeting, on Mechanical Behavior of Graphite for High temperature Reactors. Gif sur Yvette, France, pp. 96–102.

Zhang, K.S., Bai, J.B., Francois, D., 1999. Ductile fracture of materials with high void volume fraction. International Journal of Solids and Structures 36, 3407–3425.

Zhukov, A.A., Ramachandra, R.P., 1994. New findings in carbon chemistry and their relation to cast irons. Indian Foundry Journal, 13–18.